Penetration depth and gap structure in the antiperovskite oxide superconductor $Sr_{3-x}SnO$ revealed by μSR

Atsutoshi Ikeda,[1,*,†] Zurab Guguchia,[2,*,‡] Mohamed Oudah,[3,1] Shun Koibuchi,[1] Shingo Yonezawa,[1] Debarchan Das,[2] Toni Shiroka,[2] Hubertus Luetkens,[2] and Yoshiteru Maeno[1]

[1]*Department of Physics, Kyoto University, Kyoto 606-8502, Japan*

[2]*Laboratory for Muon Spin Spectroscopy, Paul Scherrer Institute, 5232 Villigen, Switzerland*

[3]*Stewart Blusson Quantum Matter Institute, University of British Columbia, Vancouver, British Columbia, Canada V6T 1Z4*

(Received 29 December 2019; revised manuscript received 23 March 2020; accepted 24 March 2020; published 4 May 2020)

We report a μSR study on the antiperovskite oxide superconductor $Sr_{3-x}SnO$. By using transverse-field μSR, we observed an increase of the muon relaxation rate upon cooling below the superconducting transition temperature $T_c = 5.4$ K, evidencing bulk superconductivity. The exponential temperature dependence of the relaxation rate σ at low temperatures suggests a fully gapped superconducting state. We evaluated the zero-temperature penetration depth $\lambda(0) \propto 1/\sqrt{\sigma(0)}$ to be around 320–1020 nm. Such a large value is consistent with the picture of a doped Dirac semimetal. Moreover, we established that the ratio $T_c/\lambda(0)^{-2}$ is larger than those of ordinary superconductors and is comparable to those of unconventional superconductors. The relatively high T_c for small carrier density may hint at an unconventional pairing mechanism beyond the ordinary phonon-mediated pairing. In addition, zero-field μSR did not provide evidence of broken time-reversal symmetry in the superconducting state. These features are consistent with the theoretically proposed topological superconducting state in $Sr_{3-x}SnO$, as well as with ordinary s-wave superconductivity.

DOI: 10.1103/PhysRevB.101.174503

I. INTRODUCTION

Antiperovskite (inverse perovskite) oxides A_3BO are materials crystallizing in the same structure as the ordinary perovskite oxides, but with the reversed positions of the metal and oxygen [1]: in antiperovskite oxides, oxygen is at the center of OA_3 octahedra. When A is an alkaline-earth element and B is a group 14 element, one can expect the ionic configuration $(A^{2+})_3B^{4-}O^{2-}$ with a metallic B anion such as Sn^{4-} or Pb^{4-}, which is rare in oxides. Indeed, this unusual metallic anion is directly observed in Sr_3SnO by recent studies of Mössbauer spectroscopy [2,3].

There has been a number of investigations toward clarifying their peculiar electronic band structure [2–18]. Theoretical calculations suggest a band inversion between the valence B-p and conduction A-d bands in some antiperovskite oxides containing heavy elements such as Ca_3PbO and Ba_3SnO. Due to this band inversion, these materials belong to the Dirac semimetals, or to the topological crystalline insulators with slightly gapped Dirac cones in the vicinity of the Fermi level of the bulk electronic states [4–6,11]. Especially, Sr_3SnO is suggested to be in the vicinity of a topological transition with barely inverted bands [6,12]. Signatures of Dirac electrons have been observed experimentally in various antiperovskite oxides including Ca_3PbO [10], Sr_3PbO [14], and Sr_3SnO [16].

Recently, some of the present authors discovered that $Sr_{3-x}SnO$ is the first superconductor among antiperovskite oxides [9]. Theoretical analyses suggested that the inverted band structure in Sr_3SnO can lead to topological superconductivity with a high winding number originating from electrons with a total angular momentum $J = 3/2$ [15]. In this theory, besides the ordinary s-wave superconductivity, unconventional superconductivities with a full gap and a point-nodal gap are suggested.

For investigations of the symmetry of the superconducting order parameter, the muon-spin relaxation/rotation (μSR) technique is a powerful tool. The London penetration depth λ can be evaluated from the muon-spin depolarization rate σ, measured in the vortex state of a type-II superconductor. We can deduce the structure of the superconducting gap from the temperature dependence of λ at temperatures much below the superconducting critical temperature T_c: in fully gapped superconductors, $\Delta\lambda^{-2}(T) = \lambda^{-2}(0) - \lambda^{-2}(T)$ exhibits an exponential temperature T dependence, whereas in nodal superconductors this quantity exhibits a power-law temperature dependence at low temperature [19]. Moreover, time-reversal-symmetry breaking of superconductivity can be detected by a change in the zero-field muon-spin depolarization rate Λ, below T_c, measured in zero magnetic field [20].

In this paper, we report μSR results on the antiperovskite oxide superconductor $Sr_{3-x}SnO$. We observe a clear increase of the transverse-field muon spin depolarization rate σ below T_c, which exhibits exponential behavior at low temperatures, indicating the absence of nodes in the superconducting gap. The deduced London penetration depth for $T \to 0$ is

*These authors contributed equally.
†a.ikeda@scphys.kyoto-u.ac.jp
‡zurab.guguchia@psi.ch

320–1020 nm and the ratio $T_c/\lambda(0)^{-2}$ is comparable to those of high-temperature superconductors. This fact possibly indicates an unconventional pairing mechanism. We also performed μSR at zero field and did not detect a breaking of the time-reversal symmetry. These results are consistent with the theoretically proposed unconventional superconductivity belonging to the same symmetry as the Balian-Werthamer (BW) state [21], as well as with the ordinary *s*-wave superconductivity [15].

II. EXPERIMENT

A. Sample preparation and characterization

Polycrystalline samples of $Sr_{3-x}SnO$ were prepared from Sr (Sigma-Aldrich, 99.99%) and SnO (Sigma-Aldrich, 99.99%). Three samples were used for the μSR studies: sample A for the measurements down to 1.5 K and samples B and C to 0.26 K. They were synthesized in the procedure same as method B described in Ref. [13]. We confirmed that the samples are dominated by $Sr_{3-x}SnO$ [7] with the lattice parameters of $a = 0.51429(4)$ nm in sample A, $a = 0.51435(3)$ nm in sample B, and $a = 0.51421(4)$ nm in sample C. These lattice parameter values were extracted from the powder x-ray diffraction (PXRD) patterns, as described in our previous report [2]. Although it is not easy to determine the actual composition of the samples accurately, we expect that x is close to 0.5 because our previous study shows that the average Sr/Sn ratio is roughly 2.5 based on energy-dispersive x-ray spectroscopy [13]. The sample for the specific-heat measurement (sample D) was prepared from the stoichiometric ratio of Sr (Furuuchi, 99.9%) and SnO (Furuuchi, 99.9%) in the procedure same as method A described in Ref. [13].

B. Magnetic susceptibility and specific heat

Direct-current (dc) magnetization was measured with a commercial magnetometer using the superconducting quantum interference device (Quantum Design, MPMS-XL). We used powder samples that were sealed in plastic capsules inside an argon-filled glovebox. Alternating-current (ac) magnetic susceptibility was measured via the mutual inductance method using a lock-in amplifier (Stanford Research Systems, SR830) and using an adiabatic demagnetization refrigerator on a commercial apparatus (Quantum Design, PPMS) [22]. Heat capacity of a sintered chunk was measured using a ^{3}He refrigerator on PPMS.

C. μSR

For μSR, we used pellets with a diameter of 10 mm. Measurements on sample A were performed at the GPS spectrometer (πM3 beamline) at the Paul Scherrer Institute (PSI) down to 1.5 K. The pellet was sealed in a polyethylene bag with a thickness of 0.1 mm under argon atmosphere in order to avoid direct contact to air. Measurements on samples B and C were carried out at the Dolly spectrometer (πE1 beamline) at PSI down to 0.26 K. Sample pellets were placed on 25-μm-thick Cu foils with grease (Apiezon, N Grease) to achieve a good thermal contact and sealed with a polyimide film (Du Pont, Kapton) under nitrogen atmosphere. The pellets of samples B and C were mounted on the cryostat using a portable glovebox with a continuous flow of nitrogen. The typical integration time of μSR was 1.5 h for each temperature and field condition.

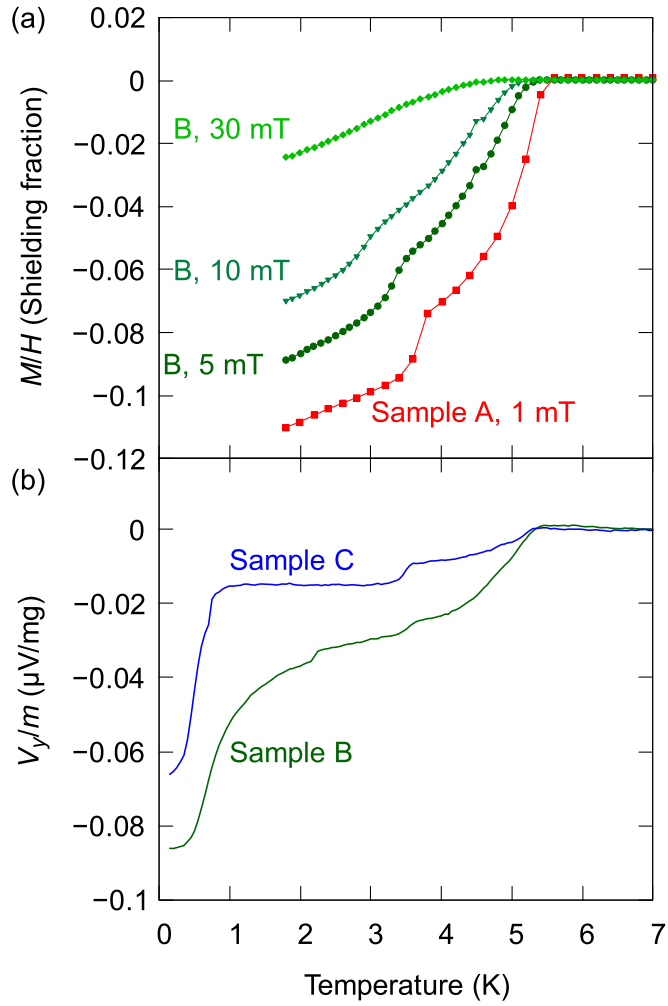

FIG. 1. (a) dc magnetic susceptibility of sample A measured at 1 mT and that of sample B at 5, 10, and 30 mT. Both samples exhibit strong diamagnetism below $T_c \simeq 5.4$ K of $Sr_{3-x}SnO$ with the shielding fractions of around 10% at 2 K. The kink at 3.7 K originates from superconductivity of Sn impurity. (b) Voltage signal detected with a mutual inductance coil normalized by the sample mass (corresponding to the real part of the ac susceptibility) of samples B and C. For both sets of data, the measurements were performed under an ac field with the amplitude of 16 μT and the frequency of 3011 Hz. Both samples exhibit superconducting transition at $T_c \simeq 5.3$ K and 0.8 K. Sample C exhibits a weaker 5-K transition but a sharper 0.8-K transition than sample B.

III. RESULTS

A. Magnetic susceptibility and specific heat

First, we show the dc magnetic susceptibility of the $Sr_{3-x}SnO$ samples in Fig. 1. All samples exhibit superconductivity at around 5.4 K. We call this primary superconducting phase the 5-K phase. The kink at 3.7 K is attributable to the superconductivity of Sn impurity, which was barely

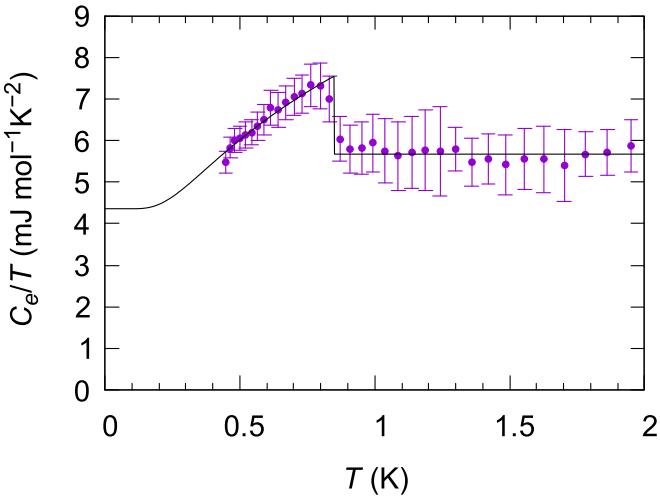

FIG. 2. Electronic specific heat divided by temperature C_e/T. We observed a clear superconducting transition at 0.85 K with a volume fraction of 23%, evidencing bulk superconductivity. The solid curve represents the fitting with the BCS theory.

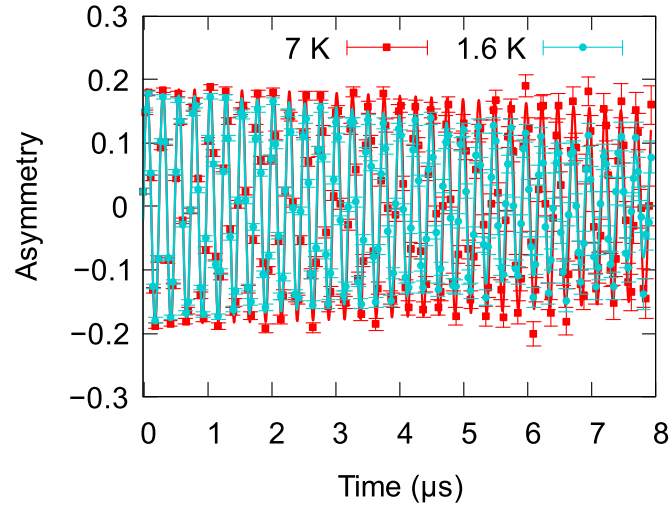

FIG. 3. Transverse-field μSR spectra for sample A at 30 mT and 7 K (red squares) and 1.6 K (blue circles). The oscillation of the asymmetry decays faster at 1.6 K than at 7 K due to the spatial distribution of the local magnetic field caused by flux-lattice formation. The solid curves are results of the fittings with the Gaussian cosine function.

seen in PXRD patterns. For sample A, the superconducting volume fraction evaluated from the dc susceptibility without the demagnetization correction reaches 11% at 1.8 K. In the case of sample B, the volume fraction is 9% at 5 mT and the fraction decreases with increasing the field. Considering that the fields applied during the measurements of sample B are stronger, we expect that the superconducting volume fraction of the 5-K phase is almost the same in both samples. The volume fraction smaller than 100% is attributable to the phase separation into multiple compositions with different amounts of Sr deficiency [2,16]. The onset of the transition decreases to 4.9 K at 30 mT. Figure 1(b) shows the ac susceptibility down to 0.2 K of samples B and C measured at zero dc field. Both samples exhibit additional superconducting transition at around 0.8 K as reported [9]. We hereafter call this second superconducting phase the 0.8-K phase. The origin of the 0.8-K phase is not clear yet, but the separation into two phases with slightly different amounts of the Sr deficiency may cause such splitting of the transitions [2]. From these results, we infer that sample B contains more 5-K phase than the 0.8-K phase, whereas sample C contains more 0.8-K phase. Sample D has a diamagnetic ratio between 5-K and 0.8-K phases similar to sample C, or sample D is dominated by the 0.8-K phase. Thus, comparing the μSR results of these samples, we may unveil the difference in the superconducting properties of the 5-K and 0.8-K phases.

Next, we present in Fig. 2 the electronic specific heat C_e divided by temperature T of sample D at low temperature. We observed a clear anomaly at around 0.85 K. We fitted the temperature dependence using the Bardeen-Cooper-Schrieffer (BCS) theory [24] and the phononic contribution, which is already subtracted in Fig. 2. We fixed $T_c = 0.85$ K to satisfy the entropy balance. We obtained the Sommerfeld coefficient $\gamma = 5.67(3)$ mJ mol^{-1}K^{-1}, the Debye temperature $\Theta_D = 119.9(2)$ K, and the volume fraction of 23%. This fact evidences the bulk nature of the 0.8-K phase.

B. μSR at 30 mT

Figure 3 compares the μSR time spectra, recorded above and below T_c, measured under an applied field of 30 mT for sample A. The presence of the randomly oriented nuclear moments causes a weak relaxation of the μSR signal above T_c. The relaxation rate is enhanced below T_c, which is caused by the formation of a flux-line lattice in the superconducting state, giving rise to an inhomogeneous magnetic field distribution. Assuming the Gaussian distribution for the probability $n(B)$ that a muon stops at a position with a local flux density of B, we fitted the data with the Gaussian cosine function

$$A(t) = A(0)\exp\left(-\frac{\sigma^2 t^2}{2}\right)\cos(2\pi\gamma_\mu B_0 t + \phi), \qquad (1)$$

where $A(0)$ and ϕ are the asymmetry and phase at $t = 0$, respectively, γ_μ is the gyromagnetic ratio of muon, and B_0 is the mean flux density inside the sample. σ changes from 0.084(6) μs^{-1} at 7 K to 0.160(4) μs^{-1} at 1.6 K. This change in σ is readily seen in the raw data, namely the faster damping at 1.6 K. The change in the relaxation rate across T_c indicates that a large portion of the muons stopped at the superconducting region of the sample.

We measured σ as a function of the applied field at 1.5 K and 3.5 K (see Fig. 4). Each point was obtained by field cooling the sample from above T_c to each measurement temperature. First, σ strongly increases with increasing magnetic field until reaching a maximum at 15 mT and then above it continuously decreases up to the highest field (100 mT) investigated. The observed field dependence of σ implies that for a reliable determination of the penetration depth, the applied field must be just above the peak. Thus we measured the temperature dependence of σ at 30 mT.

The temperature dependence of σ for sample C under an applied field of 30 mT is shown in Fig. 5. An increase of σ was observed below $T_c = 6$ K. The relaxation rate is related

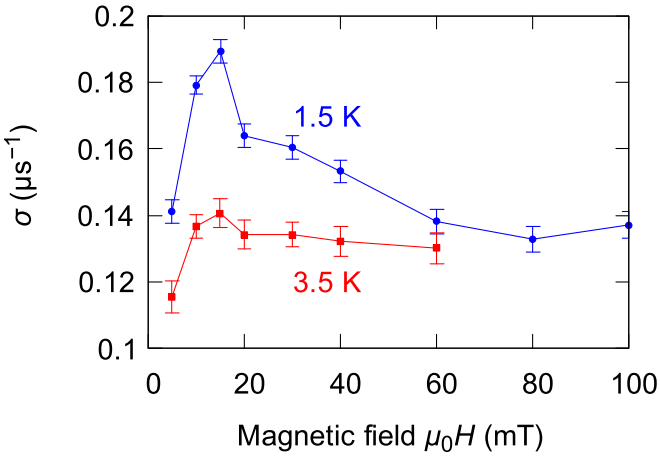

FIG. 4. Muon spin depolarization rate σ of sample A as a function of the applied magnetic field measured at 3.5 K (red squares) and 1.5 K (blue circles). The enhancement of σ below 20 mT and at 1.5 K are attributable to the superconductivity of Sn impurity with $H_c = 30.9$ mT at $T = 0$ K [23].

to the London penetration depth $\lambda(T)$ via

$$\sigma_{SC}(T) = \sqrt{0.00371} \times \frac{2\pi\gamma_\mu\Phi_0}{\lambda^2(T)}, \tag{2}$$

where $\sigma_{SC}(T) = \sqrt{\sigma^2(T) - \sigma_N^2}$ is the increase of the relaxation rate due to superconductivity, σ_N is the relaxation rate in the normal state (mostly attributable to the nuclear contribution), and Φ_0 is the flux quantum [25]. Moreover, the temperature dependence of λ for the isotropic as well as anisotropic superconducting gaps can be calculated using the BCS theory:

$$\frac{\lambda^{-2}(T)}{\lambda^{-2}(0)} = 1 + \frac{1}{2\pi}\iint_0^\infty \frac{\partial f_k}{\partial E_k} d\varepsilon\, d\hat{\boldsymbol{k}}, \tag{3}$$

where $f_k = \{1 + \exp[E_k/(k_B T)]\}^{-1}$ is the Fermi distribution function, k_B is the Boltzmann constant, and $E_k = \sqrt{\varepsilon^2 + \Delta_k^2(T)}$ is the quasiparticle excitation energy of the superconducting state with the kinetic energy ε relative to the Fermi energy ε_F and the superconducting gap $\Delta_k(T) = \Delta_0(T)Y(\hat{\boldsymbol{k}})$ [24]. The temperature dependence of Δ_0 is obtained by solving the gap equation [26]

$$\frac{1}{4\pi}\iint_0^{\varepsilon_c} \frac{1}{E_k}\tanh\left(\frac{E_k}{2k_B T}\right) Y^2(\hat{\boldsymbol{k}}) d\epsilon\, d\hat{\boldsymbol{k}} = \text{const}, \tag{4}$$

where ε_c is a cutoff energy. The constant value in the right-hand side is numerically obtained by substituting $T = T_c$ and $\Delta_0 = 0$. We simply set the cutoff energy and the Fermi energy as $\varepsilon_c = 100 k_B T_c$ and $\varepsilon_F = 2000 k_B T_c$. These values are compared to the Debye temperature $\varepsilon_D = 35 k_B T_c$ measured by ^{119}Sn-Mössbauer spectroscopy [3] and $\varepsilon_F = 2000 k_B T_c$ estimated from the band structure calculation [12].

We calculated the temperature dependence of the relaxation rate assuming two superconducting gap structures on a spherical Fermi surface: $Y(\hat{\boldsymbol{k}}) \equiv 1$ for a fully gapped and $Y(\hat{\boldsymbol{k}}) = \sqrt{\hat{k}_x^2 + \hat{k}_y^2}$ for a point-nodal state. While σ saturates at low temperatures for a fully gapped state (the solid curve in Fig. 5), σ continues to increase as lowering temperature for a point-nodal state (the dashed curve). Both fitting curves reasonably match the experimental result within the experimental error, but the root mean square error is smaller for the fully gapped state (1.2758) than for the point-nodal state (1.3933). Although it is theoretically suggested that the superconductivities with a full gap and point nodes have similar transition temperatures [15], this fitting analysis suggests that the fully gapped superconductivity such as the ordinary *s*-wave superconductivity or the topological superconductivity resembling the BW state is more likely to be realized in $Sr_{3-x}SnO$.

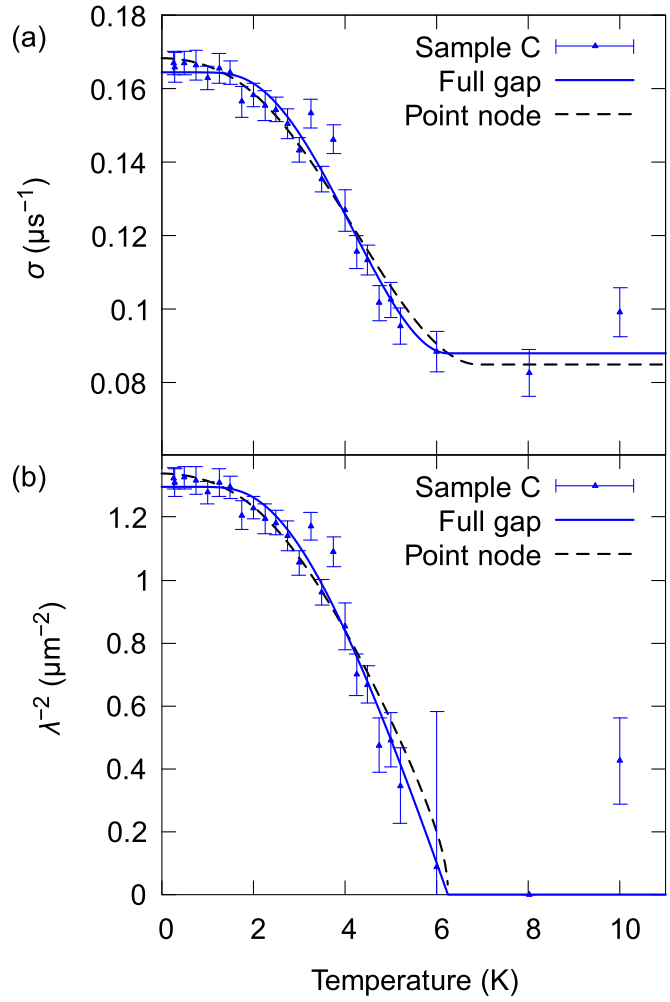

FIG. 5. Temperature dependence of (a) the muon spin depolarization rate σ and (b) the penetration depth λ for sample C at 30 mT. The solid and dashed curves represent fitting results using the theoretical formulas for the fully gapped and point-nodal superconductors, respectively. The fitting curve for the fully gapped state reproduces the experimental results better. Note that the fitting gives a T_c of 6.2 K, somewhat higher than the bulk T_c of 5.4 K.

Figure 6 compares $\sigma(T)$ of all samples measured at 30 mT. We fitted $\sigma(T)$ assuming a fully gapped superconducting wave function. The resulting values of T_c and $\lambda(0)$ are summarized in Table I. For all samples, we obtained higher T_c than those in the magnetic measurements in Fig. 1, probably because μSR detects the superconducting transition of a small

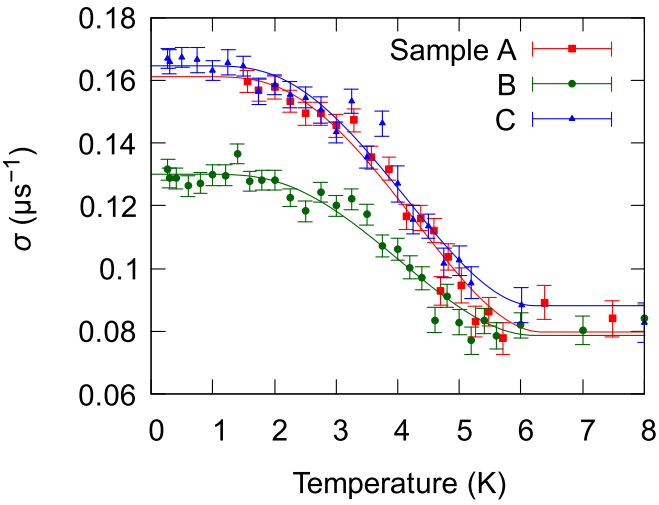

FIG. 6. Temperature dependence of the muon spin depolarization rate at 30 mT. The red squares, green circles, and blue triangles are the data for samples A, B, and C, respectively. The curve on each set of data represents the result of the fit assuming a fully gapped superconducting state.

part of the sample with slightly higher T_c. Using the coherence length of $\xi(0) = 27$ nm evaluated from the upper critical field [9], the Ginzburg-Landau parameter κ is estimated to be $\kappa = \lambda(0)/\xi(0) = 32$–$38$, suggesting a strong type-II superconductivity.

λ^{-2} is related to the superfluid density n_S and the effective mass m^* through the equation

$$\lambda^{-2} = \frac{\mu_0 n_S e^2}{m^*} \times \frac{1}{1+\xi/l}, \tag{5}$$

where μ_0 is the magnetic permeability in vacuum, e is the elementary charge, and l denotes the mean free path [24]. Since the density of states at the Fermi energy $D(\varepsilon_F)$ is evaluated to be $D(\varepsilon_F) = 1.203(7)$ eV^{-1} per unit cell per spin from γ, the superfluid density is estimated to be $n_S = \Delta_0 \times D(\varepsilon_F) \simeq 1.76 k_B T_c D(\varepsilon_F) = 1.7 \times 10^{25}$ m^{-3}. Therefore, the effective mass is calculated to be $m^* = \mu_0 n_S e^2 \lambda^2/(1+\xi/l) < \mu_0 n_S e^2 \lambda^2$ in the clean limit. The effective mass normalized by the rest mass of the electron m^*/m_e for each sample is listed in Table I. If the samples are in the dirty limit, m^* is further reduced.

It has been known that T_c and $\lambda(0)^{-2}$ of various materials exhibit a scaling behavior with the ratio $T_c/\lambda(0)^{-2}$ depending on the class of superconductors, as summarized in the Uemura plot [27,28]. For some classes of superconductors, T_c is very high despite a small n_S. For example, hole-doped cuprates and iron-based superconductors satisfy the relation $T_c/\lambda(0)^{-2} \simeq 4$ K μm^2 [27], whereas elemental superconductors exhibit much smaller $T_c/\lambda(0)^{-2}$ of less than 0.02 K μm^2 [29]. For the low-carrier superconductors $SrTi_{1-x}Nb_xO_3$ [30] and YPtBi [31], the ratio is $T_c/\lambda(0)^{-2} = 0.267$–$0.496$ and 2.0 K μm^2, respectively. Interestingly, the obtained values of $Sr_{3-x}SnO$ [$T_c = 6$ K and $\lambda(0) = 0.9$–1 μm] give a $T_c/\lambda(0)^{-2}$ ratio close to those of high-temperature or unconventional superconductors as presented in Table I and Fig. 7. These values of $T_c/\lambda(0)^{-2}$ are between those of the high-temperature superconductors and of the topological superconductor Cu-intercalated Bi_2Se_3, for which $T_c/\lambda(0)^{-2} = 10$ K μm^2 has been reported [32]. The relatively high T_c for a small number of carriers implies an unconventional superconducting mechanism in $Sr_{3-x}SnO$.

We also performed analyses to take into account the volume fraction of the superconductivity. To do this, we fitted the time-dependent asymmetry with two Gaussian cosine functions

$$A\left[\alpha \exp\left(-\frac{\sigma^2 t^2}{2}\right) + \exp\left(-\frac{\sigma_N^2 t^2}{2}\right)\right]\cos(2\pi\gamma_\mu B_0 t + \phi), \tag{6}$$

where σ_N and ϕ are fixed to the values above 6 K and α is fixed to 0.1 for samples A and B and to 0.04 for sample C corresponding to the volume fraction of 9% and 4% estimated from the susceptibility measurements in Fig. 1, respectively. The results of the two-component fits are summarized in Table I. The T_c/λ^{-2} ratios are comparable to those of the low-carrier superconductors. This fact again indicates the relatively high T_c for a small number of carriers in $Sr_{3-x}SnO$. Thus the qualitative conclusion is still valid even if the phase separation is taken into account.

C. μSR at 5 and 0 mT

Figure 8 shows the relaxation rate of sample C at 5 mT. The jump at 3.0 K probably originates from the superconductivity of Sn. We did not detect the increase of the relaxation rate at 0.8 K, probably because the field modulation caused by the 0.8-K phase is too small at 5 mT even though the superconductivity originates from the bulk. The penetration depth of the 5-K phase at 5 mT is calculated to be $8.9(2) \times 10^{-7}$ m. This value is consistent with the one at 30 mT within the error. Since the magnetic field of 20 mT is reported to completely suppress the 0.8-K phase [2], the upper critical field of the 0.8-K phase may not be large enough for μSR. Measurement

TABLE I. Transition temperature T_c, penetration depth $\lambda(0)$, effective mass m^*/m_e, and $T_c/\lambda(0)^{-2}$ of $Sr_{3-x}SnO$ extracted from μSR experiments, as resulting from fits with single and double Gaussian-cosine functions.

Fit function	Single Gaussian cosine: Eq. (1)			Double Gaussian cosines: Eq. (6)		
Sample	A	B	C	A	B	C
T_c (K)	6.3(2)	6.2(2)	6.2(2)	5.6(3)	6.05(7)	6.04(5)
$\lambda(0)$ (nm)	875(9)	1018(11)	878(10)	316(23)	340(11)	322(15)
m^*/m_e	0.46	0.61	0.46	0.053	0.067	0.060
$T_c/\lambda(0)^{-2}$ (K μm^2)	4.8	6.4	4.8	0.56	0.70	0.62

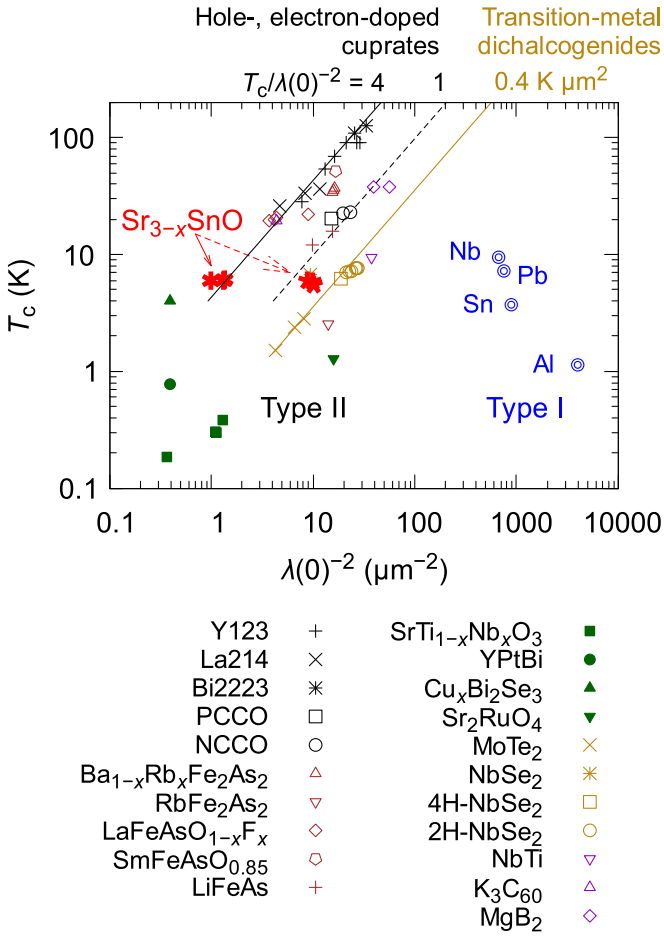

FIG. 7. Plot of T_c vs $\lambda(0)^{-2}$ (Uemura plot) for cuprate (black) [33], iron pnictide (brown) [34–38], low-carrier or unconventional (green) [30–32,39], transition-metal-dichalcogenide (orange) [19,40,41], elemental *s*-wave (blue) [29], and compound isotropic (purple) [42–45] superconductors. The solid and dashed lines represent the relations for the hole- and electron-doped cuprates and the transition metal dichalcogenides, namely $T_c/\lambda(0)^{-2} =$ 4, 1, and 0.4 K μm^2, respectively [27,46]. The large six- and five-spoked asterisks represent the data for $Sr_{3-x}SnO$ obtained from analyses with single and double Gaussian cosine functions, respectively.

of the field dependence of the relaxation rate below 0.8 K remains as a technical challenge in a future work.

Finally, we present in Fig. 9 the time dependence of the asymmetry at zero field to test a possible spontaneous time-reversal-symmetry breaking. The data were fitted with the exponential function $A\exp(-\Lambda t)$, and we obtained Λ to be 62(3) ms^{-1} at 6 K, 58(3) ms^{-1} at 1.5 K, and 63(2) ms^{-1} at 0.27 K. Thus temperature dependence of Λ is quite weak, as shown in the inset of Fig. 9. The possible maximum spontaneous flux density due to superconductivity is evaluated to be $(\Lambda_{0.27\,\mathrm{K}} - \Lambda_{6\,\mathrm{K}})/(2\pi\gamma_\mu) = 7\ \mu$T. This maximum value is seven times smaller than that observed in Sr_2RuO_4 (50 μT) [20]. Thus we conclude that the time-reversal symmetry is very likely to be preserved in the superconducting state of $Sr_{3-x}SnO$. The preserved time-reversal symmetry is consistent with the theoretically proposed topological phase as well as the ordinary *s*-wave superconductivity.

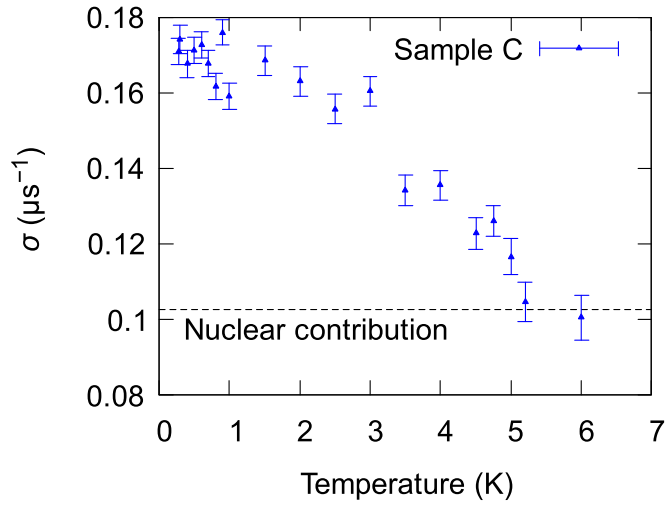

FIG. 8. Temperature-dependent relaxation rate of sample C at 5 mT. The large increase at 3 K probably originates from the superconductivity of Sn impurity.

IV. CONCLUSION

In this paper, we reported a μSR investigation of the antiperovskite oxide superconductor $Sr_{3-x}SnO$. The temperature dependence of the muon spin depolarization rate, measured in the vortex state of $Sr_{3-x}SnO$ at low temperatures, suggests a fully gapped superconductivity. The London penetration depth is estimated to be around 320–1020 nm

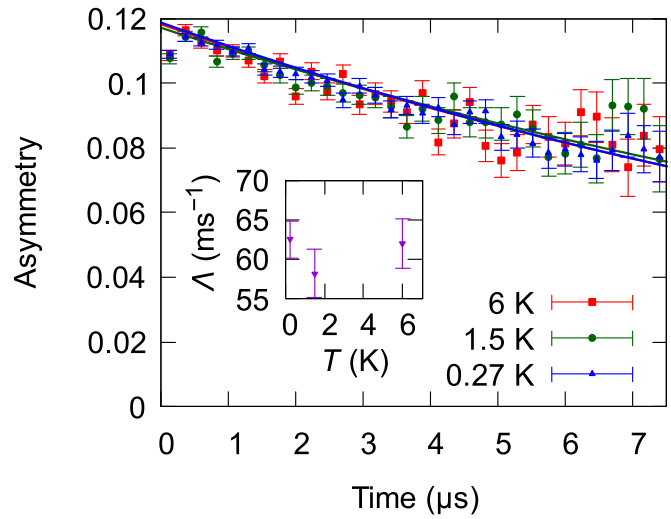

FIG. 9. Zero-field μSR spectra of sample C, recorded at 6 K (red squares), 1.5 K (green circles), and 0.27 K (blue triangles). The solid curves represent the fitting results with the exponential function. Since the signals at different temperatures are on top of each other within the error bars, the time-reversal symmetry is preserved in the superconducting state of $Sr_{3-x}SnO$. Indeed, the temperature dependence of the relaxation rate Λ is quite weak as shown in the inset.

(depending on samples and type of analysis), and the ratio $T_c/\lambda(0)^{-2}$ is similar to those of high-temperature superconductors or unusual low-carrier superconductors. This fact may hint at an unconventional superconducting mechanism in $Sr_{3-x}SnO$. In addition, we did not detect any signs of broken time-reversal symmetry. These features are consistent with the theoretically proposed topological phase, namely superconductivity similar to the B phase of ^{3}He, or with the conventional *s*-wave superconductivity.

ACKNOWLEDGMENTS

We thank Y. J. Uemura for insightful recommendations and suggestions and for helping us in planning the μSR experiments. We are grateful to C. Baines for the technical support and discussions. We also thank W. Higemoto and V. Grinenko for useful discussions. We acknowledge the Research Center for Low Temperature and Materials Sciences in Kyoto University for the supply of liquid He. This work was partially supported by Japan Society for the Promotion of Science (JSPS) KAKENHI Grants No. JP15H05851, No. JP15H05852, No. JP15K21717 (Topological Materials Science), No. JP17H04848, and No. JP17J07577, and by the JSPS Core-to-Core Program (A. Advanced Research Network), as well as by the Izumi Science and Technology Foundation (Grant No. H28-J-146). A.I. is supported by the JSPS Research Fellowship. M.O. is supported by the Max Planck-UBC-UTokyo Center for Quantum Materials.

[1] A. Widera and H. Schafer, Übergangsformen zwischen zintlphasen und echten salzen: Die verbindungen A_3BO (mit A = Ca, Sr, Ba und B = Sn, Pb), Mater. Res. Bull. **15**, 1805 (1980).

[2] M. Oudah, J. N. Hausmann, S. Kitao, A. Ikeda, S. Yonezawa, M. Seto, and Y. Maeno, Evolution of superconductivity with Sr-deficiency in antiperovskite oxide $Sr_{3-x}SnO$, Sci. Rep. **9**, 1831 (2019).

[3] A. Ikeda, S. Koibuchi, S. Kitao, M. Oudah, S. Yonezawa, M. Seto, and Y. Maeno, Negative ionic states of tin in the oxide superconductor $Sr_{3-x}SnO$ revealed by Mössbauer spectroscopy, Phys. Rev. B **100**, 245145 (2019).

[4] T. Kariyado and M. Ogata, Three-dimensional Dirac electrons at the Fermi energy in cubic inverse perovskites: Ca_3PbO and its family, J. Phys. Soc. Jpn. **80**, 083704 (2011).

[5] T. Kariyado and M. Ogata, Low-energy effective Hamiltonian and the surface states of Ca_3PbO, J. Phys. Soc. Jpn. **81**, 064701 (2012).

[6] T. H. Hsieh, J. Liu, and L. Fu, Topological crystalline insulators and Dirac octets in antiperovskites, Phys. Rev. B **90**, 081112(R) (2014).

[7] J. Nuss, C. Mühle, K. Hayama, V. Abdolazimi, and H. Takagi, Tilting structures in *inverse* perovskites, M_3TtO (M = Ca, Sr, Ba, Eu; Tt = Si, Ge, Sn, Pb), Acta Crystallogr. B **71**, 300 (2015).

[8] Y. Okamoto, A. Sakamaki, and K. Takenaka, Thermoelectric properties of antiperovskite calcium oxides Ca_3PbO and Ca_3SnO, J. Appl. Phys. **119**, 205106 (2016).

[9] M. Oudah, A. Ikeda, J. N. Hausmann, S. Yonezawa, T. Fukumoto, S. Kobayashi, M. Sato, and Y. Maeno, Superconductivity in the antiperovskite Dirac-metal oxide $Sr_{3-x}SnO$, Nat. Commun. **7**, 13617 (2016).

[10] Y. Obata, R. Yukawa, K. Horiba, H. Kumigashira, Y. Toda, S. Matsuishi, and H. Hosono, ARPES studies of the inverse perovskite Ca_3PbO: Experimental confirmation of a candidate 3D Dirac fermion system, Phys. Rev. B **96**, 155109 (2017).

[11] T. Kariyado and M. Ogata, Evolution of band topology by competing band overlap and spin-orbit coupling: Twin Dirac cones in Ba_3SnO as a prototype, Phys. Rev. Materials **1**, 061201 (2017).

[12] A. Ikeda, T. Fukumoto, M. Oudah, J. N. Hausmann, S. Yonezawa, S. Kobayashi, M. Sato, C. Tassel, F. Takeiri, H. Takatsu, H. Kageyama, and Y. Maeno, Theoretical band structure of the superconducting antiperovskite oxide $Sr_{3-x}SnO$, Physica B: Condens. Matter **536**, 752 (2018).

[13] J. N. Hausmann, M. Oudah, A. Ikeda, S. Yonezawa, and Y. Maeno, Controlled synthesis of the antiperovskite oxide superconductor $Sr_{3-x}SnO$, Supercond. Sci. Technol. **31**, 055012 (2018).

[14] S. Suetsugu, K. Hayama, A. W. Rost, J. Nuss, C. Mühle, J. Kim, K. Kitagawa, and H. Takagi, Magnetotransport in Sr_3PbO antiperovskite, Phys. Rev. B **98**, 115203 (2018).

[15] T. Kawakami, T. Okamura, S. Kobayashi, and M. Sato, Topological Crystalline Materials of $J = 3/2$ Electrons: Antiperovskites, Dirac Points, and High Winding Topological Superconductivity, Phys. Rev. X **8**, 041026 (2018).

[16] S. Kitagawa, K. Ishida, M. Oudah, J. N. Hausmann, A. Ikeda, S. Yonezawa, and Y. Maeno, Normal-state properties of the antiperovskite oxide $Sr_{3-x}SnO$ revealed by ^{119}Sn-NMR, Phys. Rev. B **98**, 100503(R) (2018).

[17] T. Kariyado, Counting Pseudo Landau levels in spatially modulated Dirac systems, J. Phys. Soc. Jpn. **88**, 083701 (2019).

[18] Y. Obata, Y. Kohama, S. Matsuishi, and H. Hosono, Shubnikov–de Haas oscillations in the three-dimensional Dirac fermion system Ca_3PbO, Phys. Rev. B **99**, 115133 (2019).

[19] Z. Guguchia, F. von Rohr, Z. Shermadini, A. T. Lee, S. Banerjee, A. R. Wieteska, C. A. Marianetti, B. A. Frandsen, H. Luetkens, Z. Gong, S. C. Cheung, C. Baines, A. Shengelaya, G. Taniashvili, A. N. Pasupathy, E. Morenzoni, S. J. L. Billinge, A. Amato, R. J. Cava, R. Khasanov, and Y. J. Uemura, Signatures of the topological s^{+-}: superconducting order parameter in the type-II Weyl semimetal T_d-$MoTe_2$, Nat. Commun. **8**, 1082 (2017).

[20] G. M. Luke, Y. Fudamoto, K. M. Kojima, M. I. Larkin, J. Merrin, B. Nachumi, Y. J. Uemura, Y. Maeno, Z. Q. Mao, Y. Mori, H. Nakamura, and M. Sigrist, Time-reversal symmetry-breaking superconductivity in Sr_2RuO_4, Nature (London) **394**, 558 (1998).

[21] R. Balian and N. R. Werthamer, Superconductivity with Pairs in a relative *p* wave, Phys. Rev. **131**, 1553 (1963).

[22] S. Yonezawa, T. Higuchi, Y. Sugimoto, C. Sow, and Y. Maeno, Compact AC susceptometer for fast sample characterization down to 0.1 K, Rev. Sci. Instrum. **86**, 093903 (2015).

[23] R. W. Shaw, D. E. Mapother, and D. C. Hopkins, Critical fields of superconducting tin, indium, and tantalum, Phys. Rev. **120**, 88 (1960).

[24] M. Tinkham, *Introduction to Superconductivity* (Dover Publications, New York, 2004).

[25] E. H. Brandt, Flux distribution and penetration depth measured by muon spin rotation in high-T_c superconductors, Phys. Rev. B **37**, 2349 (1988).

[26] K. Hasselbach, J. R. Kirtley, and J. Flouquet, Symmetry of the gap in superconducting URu_2Si_2, Phys. Rev. B **47**, 509 (1993).

[27] Y. J. Uemura, G. M. Luke, B. J. Sternlieb, J. H. Brewer, J. F. Carolan, W. N. Hardy, R. Kadono, J. R. Kempton, R. F. Kiefl, S. R. Kreitzman, P. Mulhern, T. M. Riseman, D. L. Williams, B. X. Yang, S. Uchida, H. Takagi, J. Gopalakrishnan, A. W. Sleight, M. A. Subramanian, C. L. Chien, M. Z. Cieplak, G. Xiao, V. Y. Lee, B. W. Statt, C. E. Stronach, W. J. Kossler, and X. H. Yu, Universal Correlations between T_c and n_s/m^* (Carrier Density over Effective Mass) in High-T_c Cuprate Superconductors, Phys. Rev. Lett. **62**, 2317 (1989).

[28] Y. J. Uemura, L. P. Le, G. M. Luke, B. J. Sternlieb, W. D. Wu, J. H. Brewer, T. M. Riseman, C. L. Seaman, M. B. Maple, M. Ishikawa, D. G. Hinks, J. D. Jorgensen, G. Saito, and H. Yamochi, Basic Similarities among Cuprate, Bismuthate, Organic, Chevrel-Phase, and Heavy-Fermion Superconductors Shown by Penetration-Depth Measurements, Phys. Rev. Lett. **66**, 2665 (1991).

[29] C. Kittel, *Introduction to Solid State Physics* (Wiley, New York, 2005).

[30] C. Collignon, B. Fauqué, A. Cavanna, U. Gennser, D. Mailly, and K. Behnia, Superfluid density and carrier concentration across a superconducting dome: The case of strontium titanate, Phys. Rev. B **96**, 224506 (2017).

[31] T. Bay, M. Jackson, C. Paulsen, C. Baines, A. Amato, T. Orvis, M. Aronson, Y. Huang, and A. de Visser, Low field magnetic response of the non-centrosymmetric superconductor YPtBi, Solid State Commun. **183**, 13 (2014).

[32] J. A. Krieger, A. Kanigel, A. Ribak, E. Pomjakushina, K. B. Chashka, K. Conder, E. Morenzoni, T. Prokscha, A. Suter, and Z. Salman, Superconducting properties of Cu intercalated Bi_2Se_3 studied by muon spin spectroscopy, JPS Conf. Proc. **21**, 011028 (2018).

[33] J. Kim, F. Ronning, N. Haberkorn, L. Civale, E. Nazaretski, N. Ni, R. J. Cava, J. D. Thompson, and R. Movshovich, Large magnetic penetration depth and thermal fluctuations in a superconducting $Ca_{10}(Pt_3As_8)[(Fe_{1-x}Pt_x)_2As_2]_5$ ($x = 0.097$) single crystal, Phys. Rev. B **85**, 180504(R) (2012).

[34] R. Khasanov, H. Luetkens, A. Amato, H.-H. Klauss, Z.-A. Ren, J. Yang, W. Lu, and Z.-X. Zhao, Muon spin rotation studies of $SmFeAsO_{0.85}$ and $NdFeAsO_{0.85}$ superconductors, Phys. Rev. B **78**, 092506 (2008).

[35] H. Luetkens, H.-H. Klauss, M. Kraken, F. J. Litterst, T. Dellmann, R. Klingeler, C. Hess, R. Khasanov, A. Amato, C. Baines, M. Kosmala, O. J. Schumann, M. Braden, J. Hamann-Borrero, N. Leps, A. Kondrat, G. Behr, J. Werner, and B. Buchner, The electronic phase diagram of the $LaO_{1-x}F_xFeAs$ superconductor, Nat. Mater. **8**, 305 (2009).

[36] F. L. Pratt, P. J. Baker, S. J. Blundell, T. Lancaster, H. J. Lewtas, P. Adamson, M. J. Pitcher, D. R. Parker, and S. J. Clarke, Enhanced superfluid stiffness, lowered superconducting transition temperature, and field-induced magnetic state of the pnictide superconductor LiFeAs, Phys. Rev. B **79**, 052508 (2009).

[37] Z. Shermadini, J. Kanter, C. Baines, M. Bendele, Z. Bukowski, R. Khasanov, H.-H. Klauss, H. Luetkens, H. Maeter, G. Pascua, B. Batlogg, and A. Amato, Microscopic study of the superconducting state of the iron pnictide $RbFe_2As_2$ via muon spin rotation, Phys. Rev. B **82**, 144527 (2010).

[38] Z. Guguchia, Z. Shermadini, A. Amato, A. Maisuradze, A. Shengelaya, Z. Bukowski, H. Luetkens, R. Khasanov, J. Karpinski, and H. Keller, Muon-spin rotation measurements of the magnetic penetration depth in the iron-based superconductor $Ba_{1-x}Rb_xFe_2As_2$, Phys. Rev. B **84**, 094513 (2011).

[39] T. M. Riseman, P. G. Kealey, E. M. Forgan, A. P. Mackenzie, L. M. Galvin, A. W. Tyler, S. L. Lee, C. Ager, D. M. Paul, C. M. Aegerter, R. Cubitt, Z. Q. Mao, T. Akima, and Y. Maeno, Observation of a square flux-line lattice in the unconventional superconductor Sr_2RuO_4, Nature (London) **396**, 242 (1998).

[40] L. P. Le, G. M. Luke, B. J. Sternlieb, W. D. Wu, Y. J. Uemura, J. W. Brill, and H. Drulis, Magnetic penetration depth in layered compound $NbSe_2$ measured by muon spin relaxation, Physica C: Superconductivity **185–189**, 2715 (1991).

[41] F. O. von Rohr, J.-C. Orain, R. Khasanov, C. Witteveen, Z. Shermadini, A. Nikitin, J. Chang, A. R. Wieteska, A. N. Pasupathy, M. Z. Hasan, A. Amato, H. Luetkens, Y. J. Uemura, and Z. Guguchia, Unconventional scaling of the superfluid density with the critical temperature in transition metal dichalcogenides, Sci. Adv. **5**, eaav8465 (2019).

[42] Y. J. Uemura, A. Keren, L. P. Le, G. M. Luke, B. J. Sternlieb, W. D. Wu, J. H. Brewer, R. L. Whetten, S. M. Huang, S. Lin, R. B. Kaner, F. Diederich, S. Donovan, G. Gruner, and K. Holczer, Magnetic-field penetration depth in K_3C_{60} measured by muon spin relaxation, Nature (London) **352**, 605 (1991).

[43] A. Gauzzi, J. Le Cochec, G. Lamura, B. J. Jönsson, V. A. Gasparov, F. R. Ladan, B. Plaçais, P. A. Probst, D. Pavuna, and J. Bok, Very high resolution measurement of the penetration depth of superconductors by a novel single-coil inductance technique, Rev. Sci. Instrum. **71**, 2147 (2000).

[44] X. H. Chen, Y. Y. Xue, R. L. Meng, and C. W. Chu, Penetration depth and anisotropy in MgB_2, Phys. Rev. B **64**, 172501 (2001).

[45] A. Carrington and F. Manzano, Magnetic penetration depth of MgB_2, Physica C: Supercond. **385**, 205 (2003).

[46] A. Shengelaya, R. Khasanov, D. G. Eshchenko, D. Di Castro, I. M. Savić, M. S. Park, K. H. Kim, S.-I. Lee, K. A. Müller, and H. Keller, Muon-Spin-Rotation Measurements of the Penetration Depth of the Infinite-Layer Electron-Doped $Sr_{0.9}La_{0.1}CuO_2$ Cuprate Superconductor, Phys. Rev. Lett. **94**, 127001 (2005).